GSA Data Repository Item 2019071

Fiske, R.S., Rose, T.R., Swanson, D.A., Andrews, B.J., and Nichols, A.R.L., 2019, The Kulanaokuaiki-3 tephra, 900 CE: Products of a remarkably energetic pyroclastic eruption at Kīlauea Volcano, Hawai‘i, USA: GSA Bulletin, https://doi.org/10.1130/B35063.1.

Data Repository

DR1. Tephra sections at near-summit sites likely related to K-3 deposits further south.

DR2.

DR3. Kulanaokuaiki 3 lithic collection data.

DR4.

DR5. Slicing method used for the K-3 tephra in on cm depth increments.

DR6.

DR7. XRF procedures.

DR8. FTIR analysis procedures.

Table DR8-1. Standard compositions, precision and detection limits for major elements measured on the electron microprobe for the inclusions and olivine host crystals. Precision and detection limits calculated using peak and background count rates and measuring times.

Table DR8-2. Upper K-3 deposit original inclusion and olivine host compositions.

Table DR8-3. Upper K-3 deposit original inclusion and olivine host compositions.

DR9. SEM and Microprobe procedures.

DR10.

DR11. Componentry of 2-4mm K-3 samples.

DR12.

DR13. K-3 glass compositions

DR14. Terminal velocity measurements.

DR15. Matlab model of lithic ejection via high-velocity jet.

DR-1 Tephra sections at near-summit sites likely related to K-3 deposits further south.

Locality (coordinates use Old Hawaiian Datum)	Setting	Lithologies	Interpretations
A. Mauna Loa Strip Road. *19.44437* *-155.31101*	Pit, 1.6 m deep and 1 m diameter; dug by soil scientists before our study	1-cm scoria layer @27 cm with scattered lithic lapilli and a 4-cm gabbro block at base of layer. @ 27-32 cm.2-cm scoria layer @ 20 cm; contains scattered free olivines. Section underlain by high Ti-K geochemical marker of Kulanaokuaiki 2 (K-2).	Scoria deposits and associated lithic clasts suggest affinities to episode-1 and -2 deposits south of the summit. Underlying K-2 Ti-K anomaly confirms K-3 affinity.
B. Tree Molds *19.43671* *-155.28292*	Exposure in outer wall of Kīlauea Caldera; overlain by 5-m lava flow	Three 3-cm scoria deposits. The lower two deposits contain lithic lapilli; the lowest of these yielded a 7-cm vitric bomb. The upper deposit contains abundant loose olivine crystals. Section underlain by high Ti-K geochemical marker of K- 2.	The lower and upper deposits, rich in scoria lapilli, have lithologic similarities to those of episodes 1 and 2 south of the summit. The middle layer may be the product of a K-3 event not present south of the summit. Underlying K-2 Ti-K anomaly confirms K-3 affinity..
C. Uwēkahuna Bluff *19.42446* *-155.28800*	Two exposures; one in natural outcrop at base of Bluff and the other in hand-dug pit ~30 m higher in Bluff. All three sections overlain by 90-120 m of caldera-wall lavas.	The 220-cm Bluff base sequence, contains evidence of high-energy deposition. Lower 85 cm consists of thin bedded vitric ash overlain by 53-cm of massive lithic ash containing 20-40 cm lithic blocks and bedded-ash rip-ups. Mid-Bluff deposits, 310 cm thick. Generally similar to those at Bluff base. Mid-Bluff section underlain by high Ti-K geochemical marker of K-2.	Both Bluff sections are thicker and more diverse than K-3 sections south of the summit; some units are coarser grained and more poorly sorted than those elsewhere. Underlying K-2 Ti-K anomaly suggests affinity with K-3.
D. Kīlauea Iki crater *No Lat-Long… too steep.*	Holcomb (1987) was the first to recognize two tephra exposures in the east wall of Kīlauea Iki crater, covered by lava flows ~100 m thick.	About 55 cm of tephra is exposed in the southern exposure. The basal 28 cm of oxidized spatter is overlain by 10 cm of poorly-sorted lapilli grading upward to vitric ash. Lithic lapilli are common in this unit, including a 4-cm block of coarse-grained gabbro. The section is topped by 17 cm of vitric-lithic ash and scoria. Steep cliffs prevented inspection of the northern exposure.	These deposits bear little resemblance to K-3 units south of the summit. The 10-cm layer of vitric ash and lapilli , plus lithic clasts, possibly relates to K-3. The K-2 Ti-K anomaly was not found in the lower part of the section.

Site 1

Site 2

Site 3

Site 4

Site 5

Site 6

Site 7

Site 8

Site 9

Site 10

Site 11

Site 12

Site 13

Site 14

Site 15

Site 16

Site 17

Site 18

Site 19

Site 20

Site 21

Site 22

Site 23

Site 24

Site 25

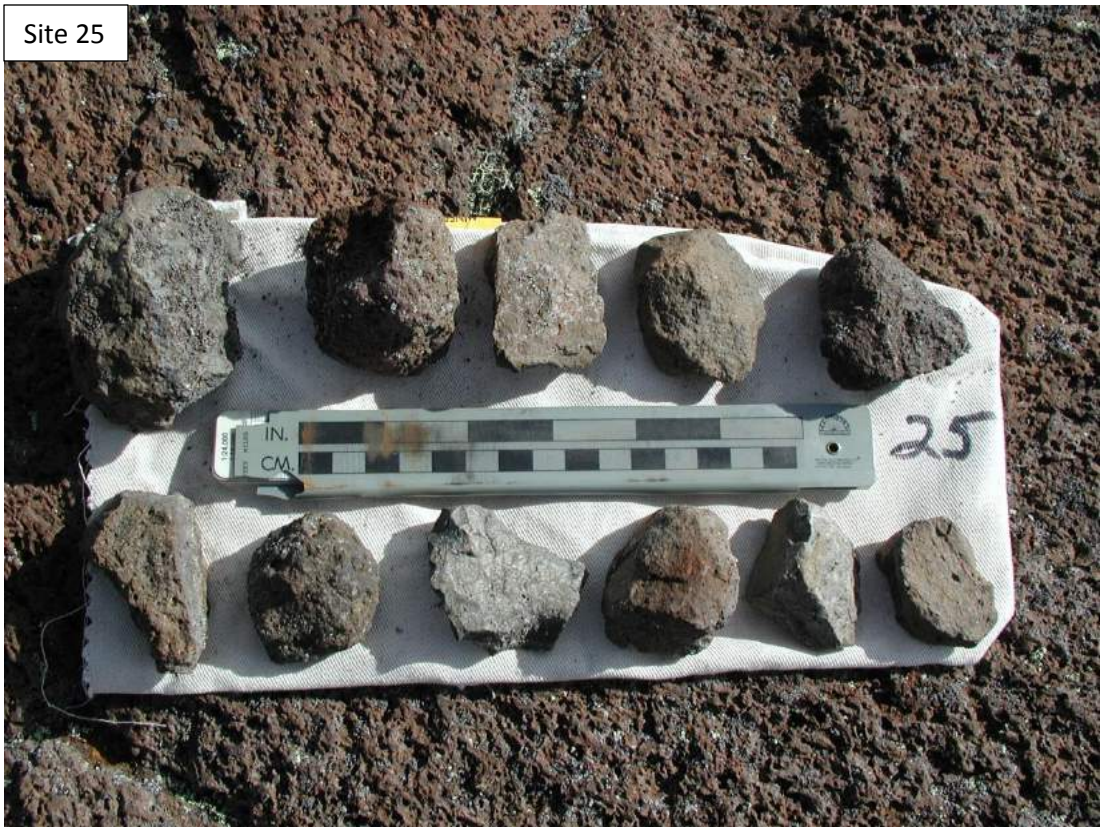

Site 26

Site 27

Site 28

Site 29

Site 30

Site 31

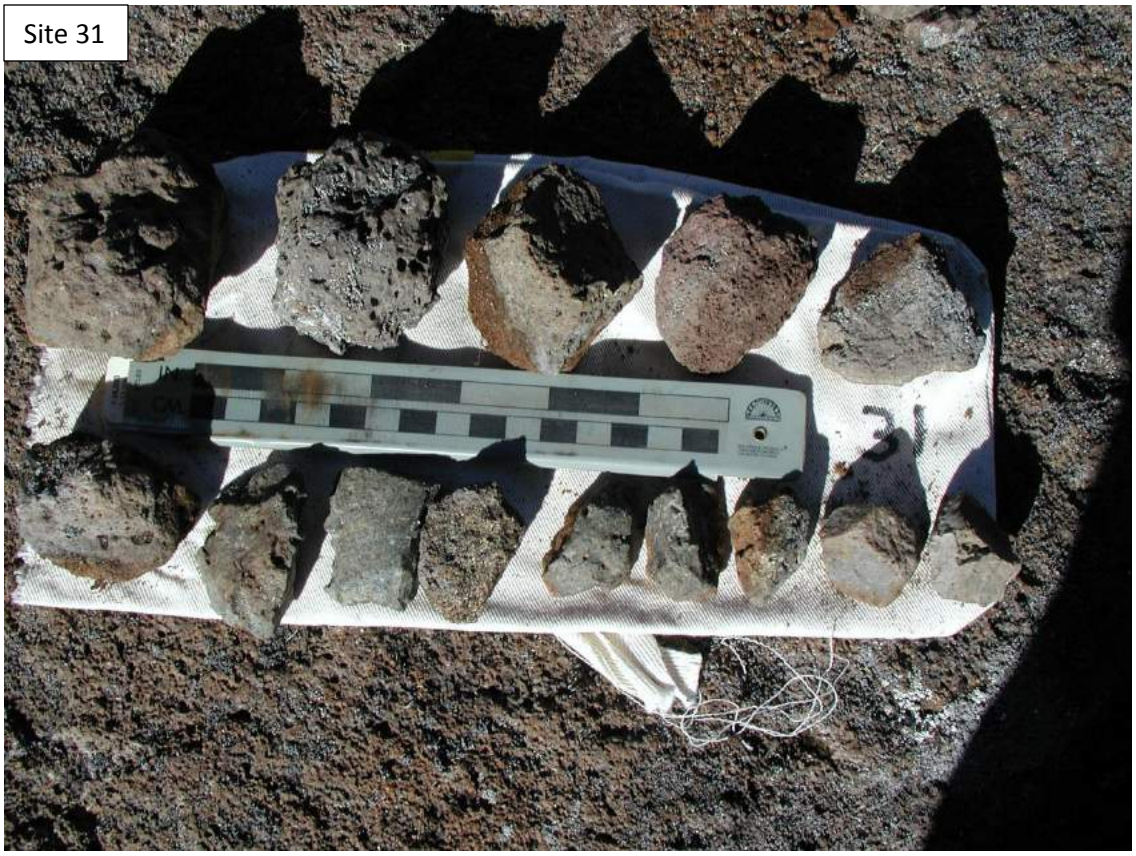

Site 32

Site 32A

Site 33

Site 34

Site 35

Site 36

Site 37

Site 41

Site 41A

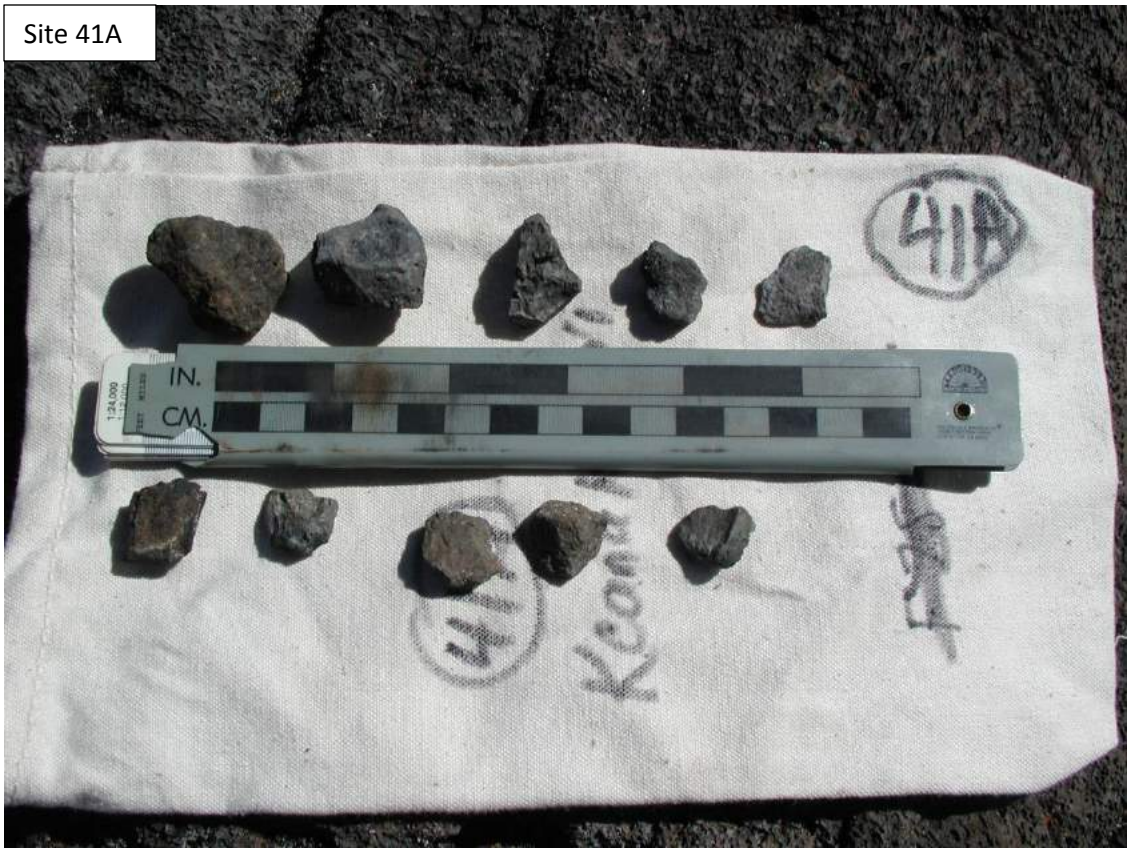

Site 42

Site 43

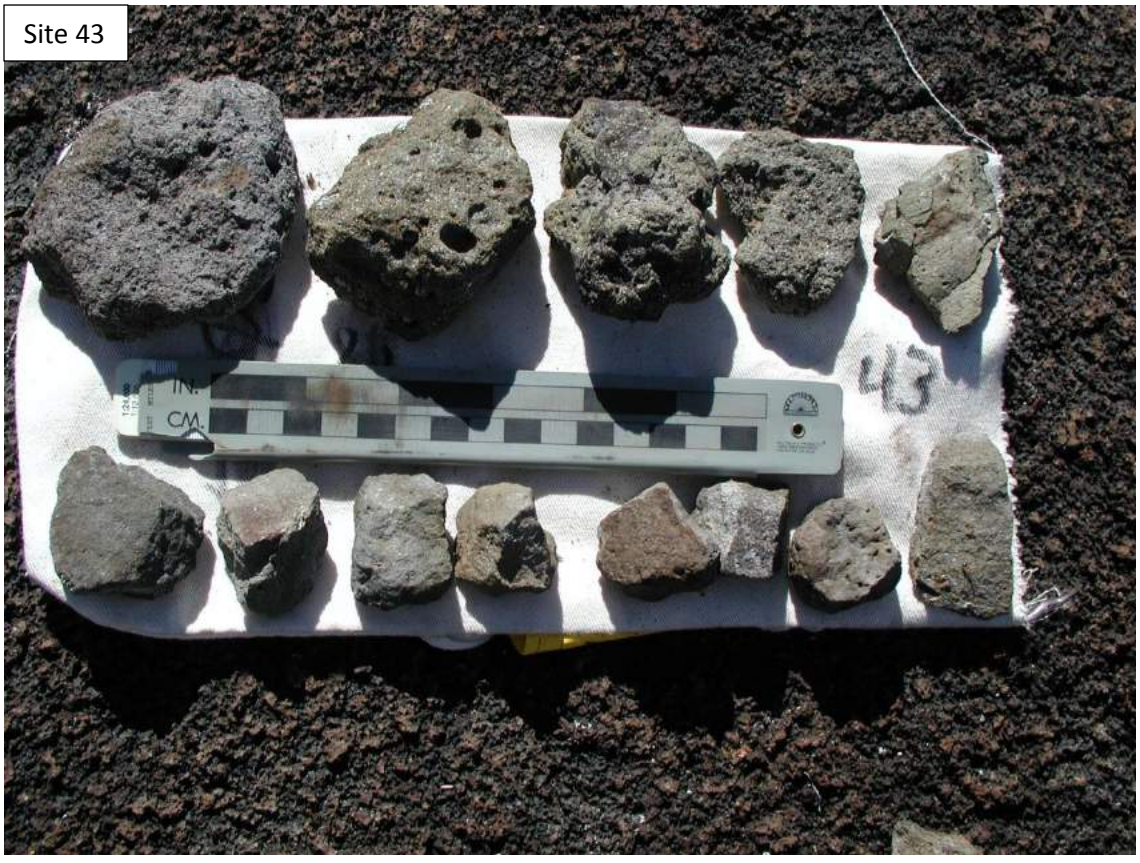

Site 44

Site 46

Site 47

Site 51

Site 52

Site 53

Site 56

Site 57

Site 58

Site 59

Site 60

Site 61

Site 62

Site 63

Site 64

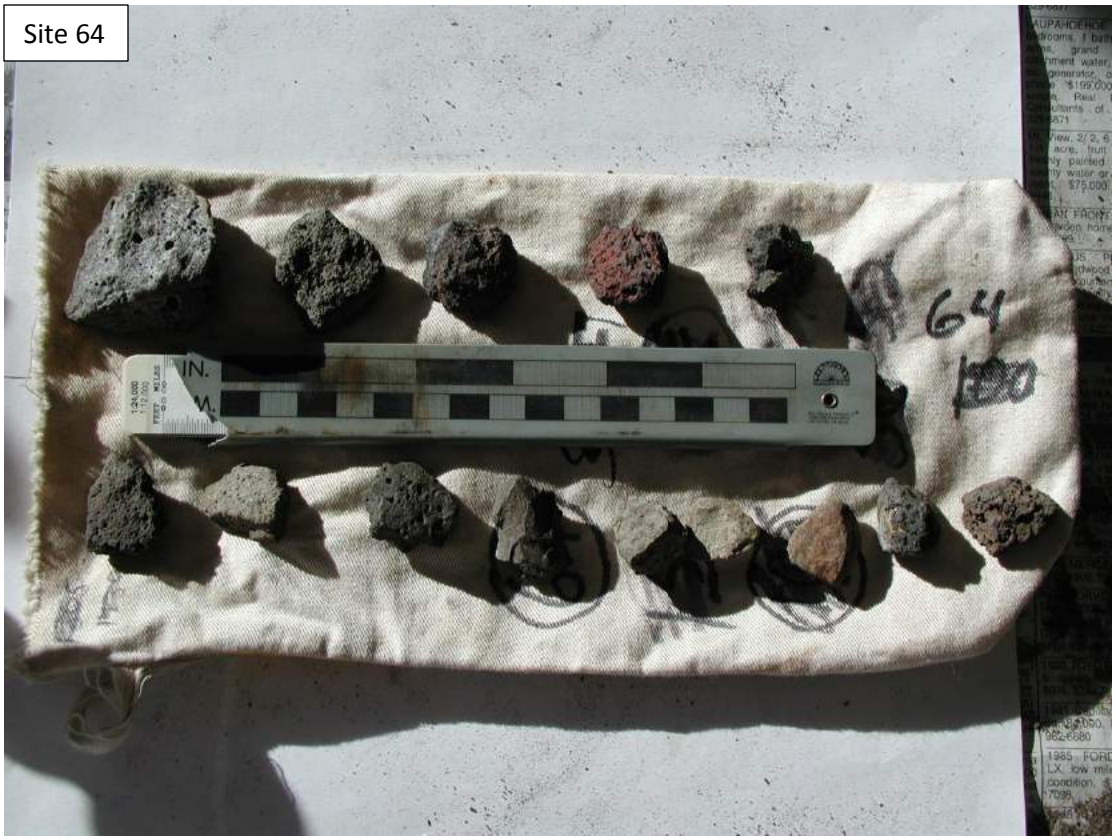

Site 65

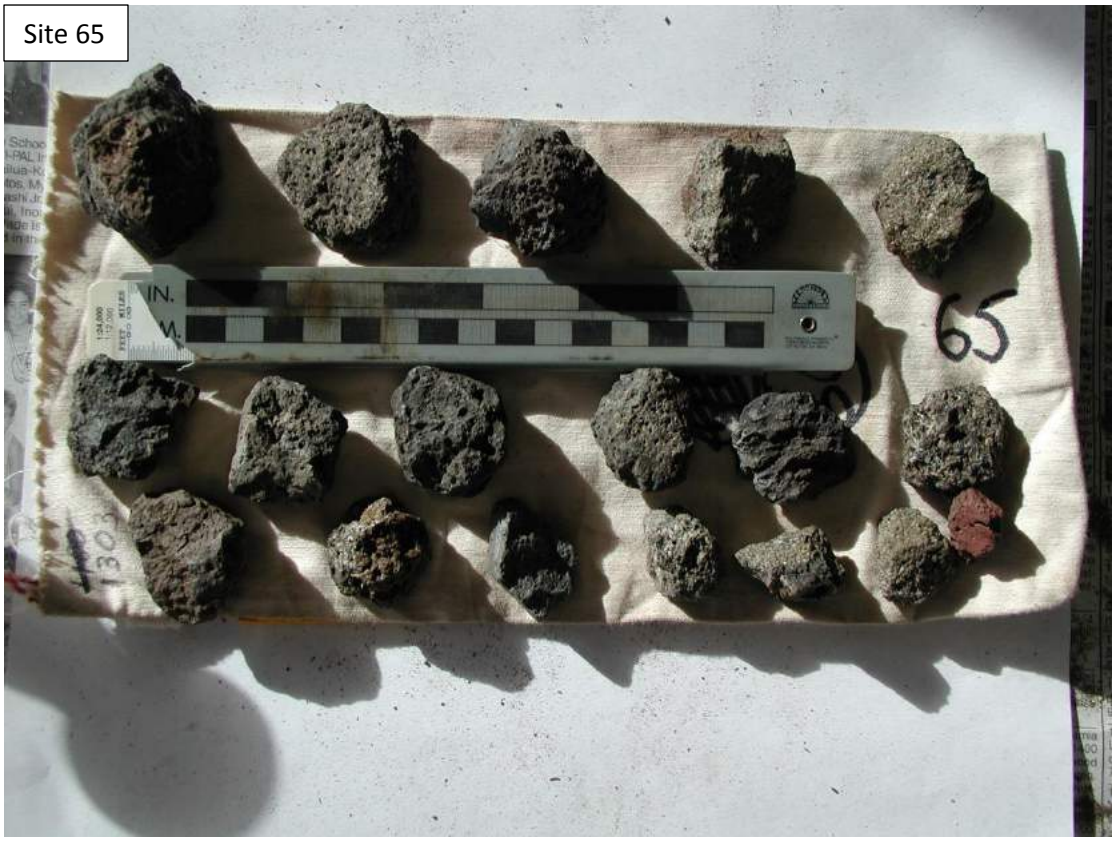

Site 66

Site 67

Site 68

Site 69

Site 70

Site 71

Site 72

Site 74

Site 75

Site 76

Site 77

Site 79

Site 80

Site 81

Site 82

Site 83

Site 84

Site 85

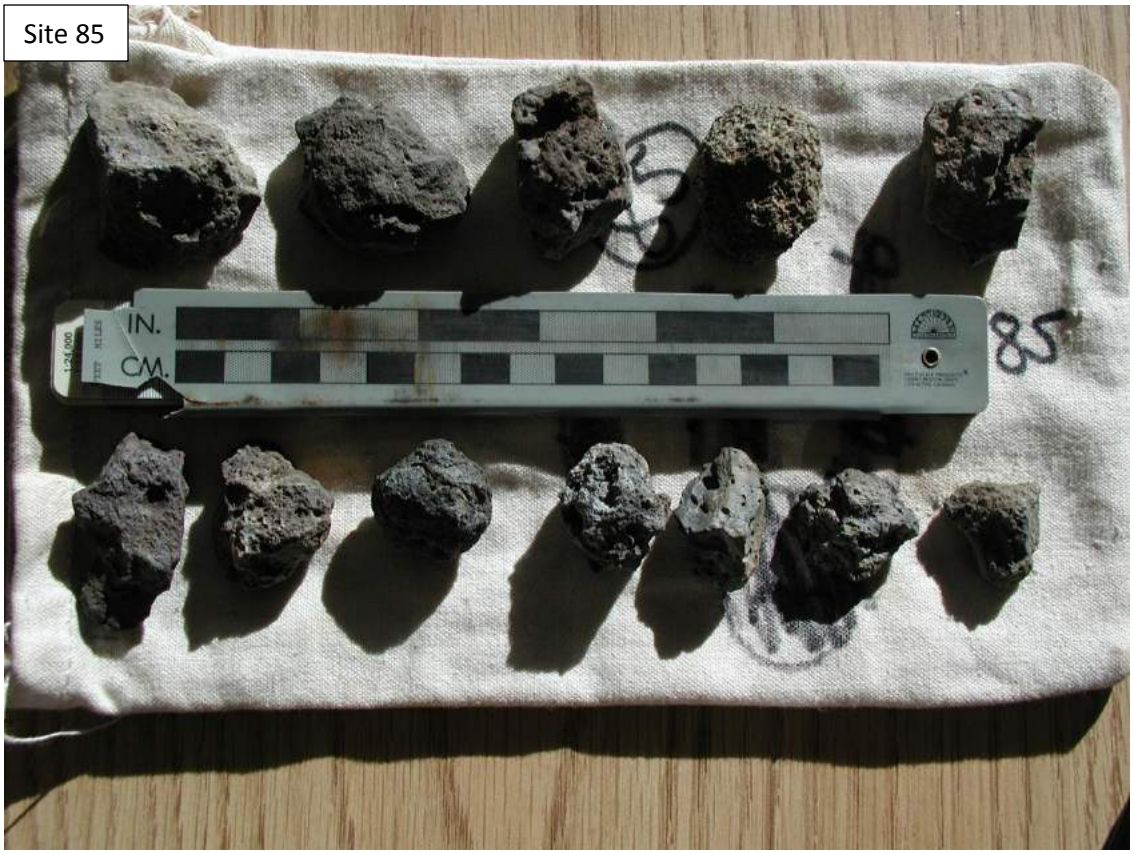

Site 86

Site 87

Site 88

Site 89

Site 90

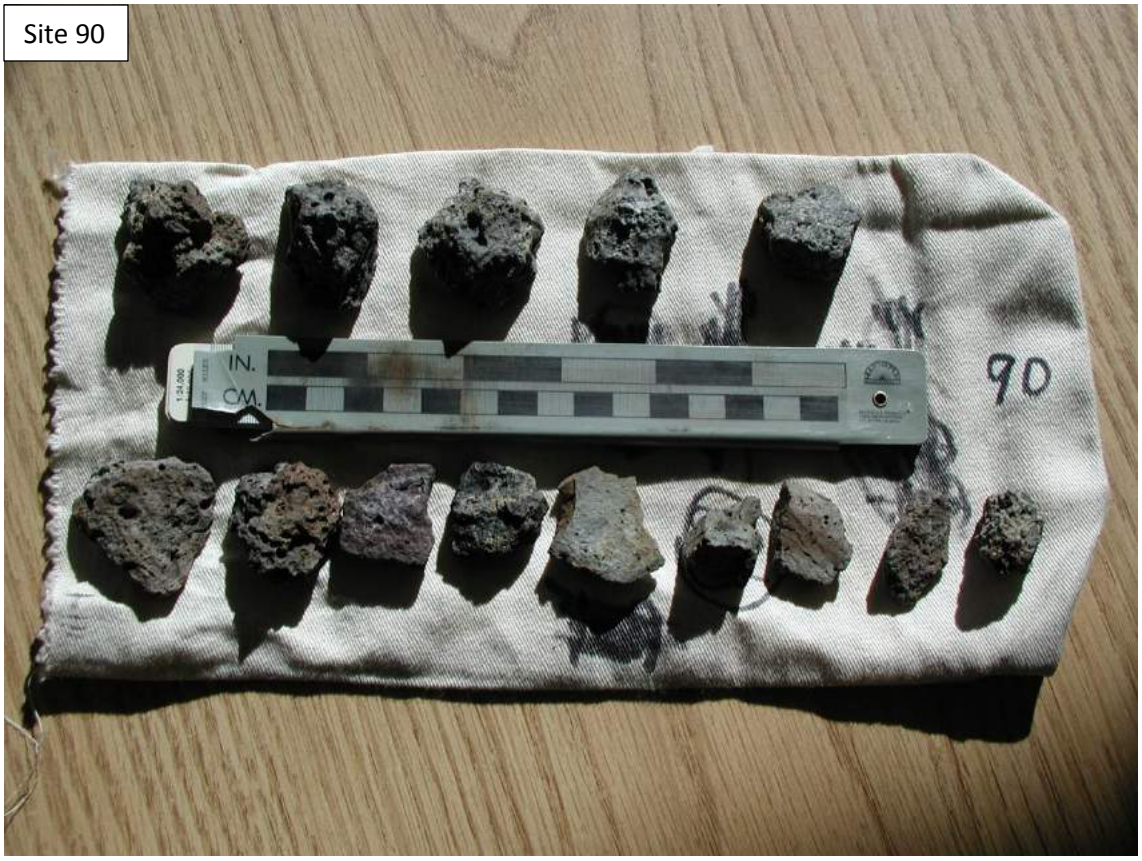

Site 91

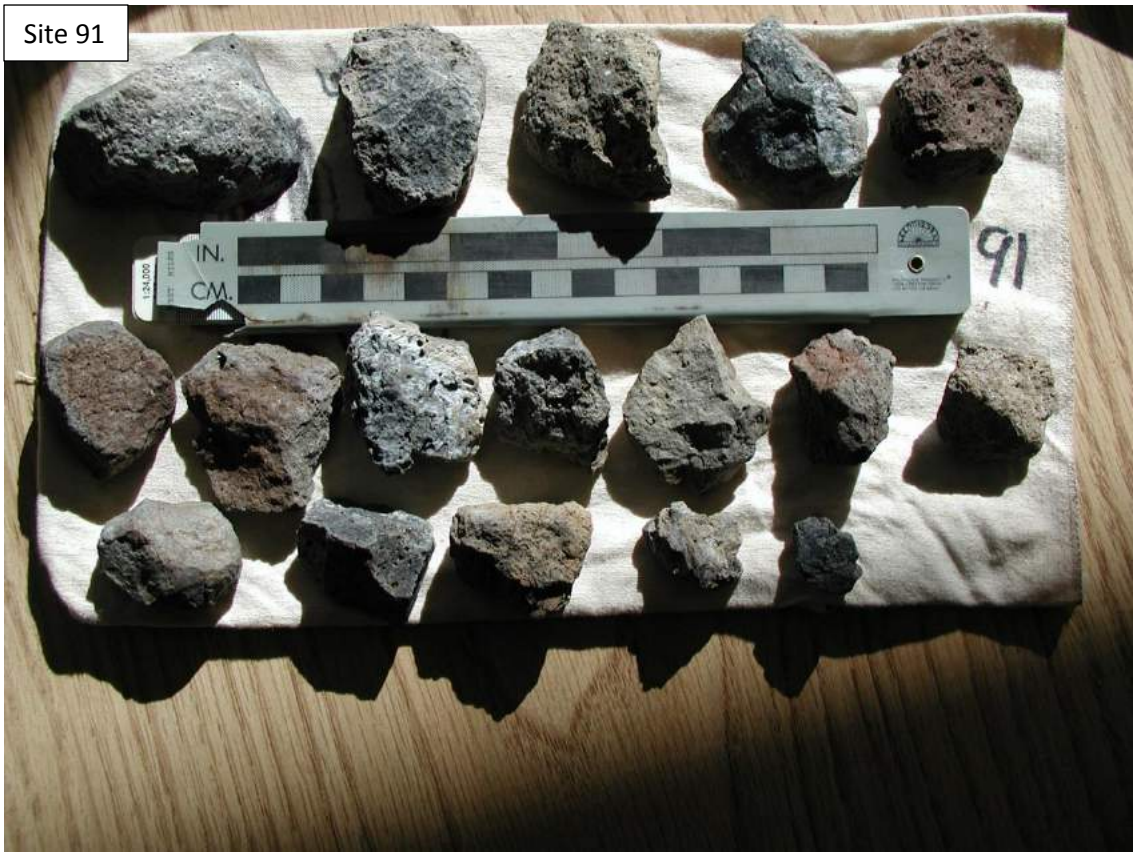

Site 92

Site 93

Site 94

Site 95

Site 97

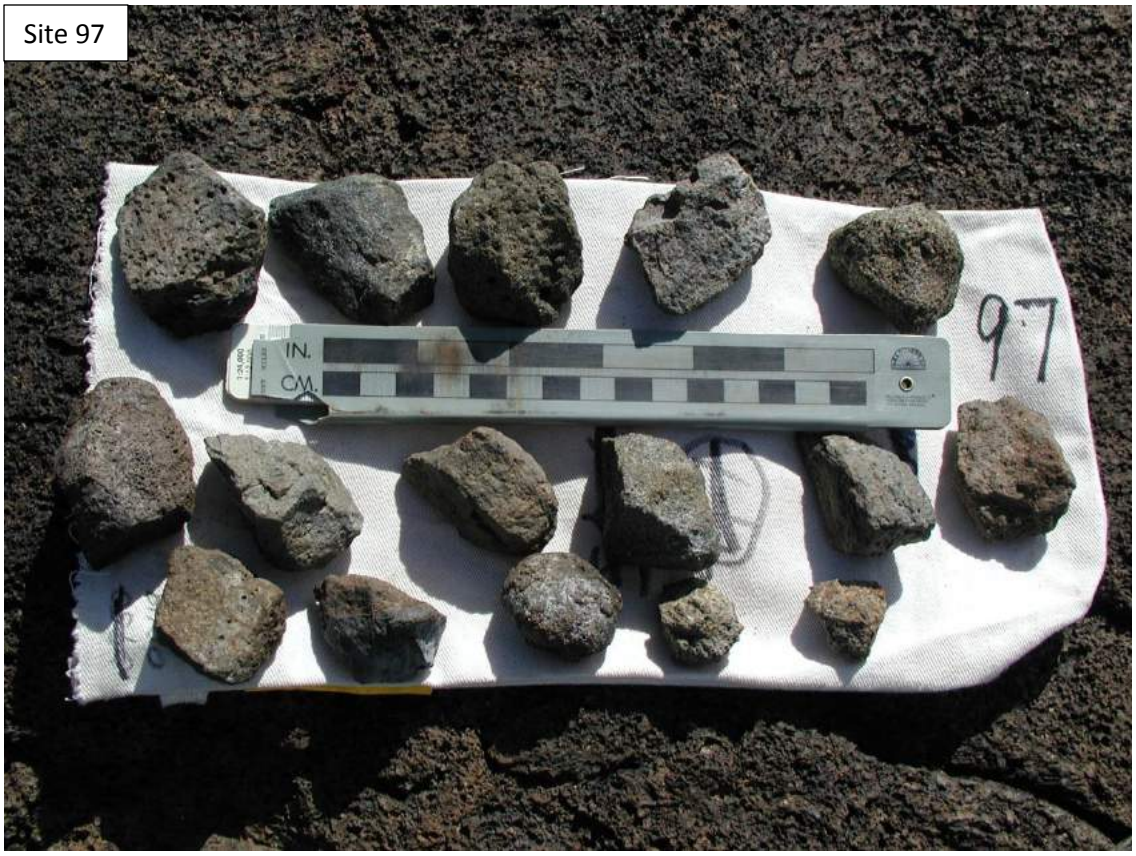

Site 98

Site 99

Site 100

Site 101

Site 102

Site 103

Site 104

Site 105

Site 111

Site 112

Site 113

Site 122

Site 124

DR-5 Slicing method used for the K-3 tephra in on cm depth increments.

A. Set of one cm thick wooden bars with pins to hold them together in a stack.
B. After exposing the top of the tephra unit, a vertical face down into the tephra is exposed. The stack of bars is placed against the face and the exposed top of the tephra is protected while the stack of bars is buttressed with soil.
C. A brush is used to expose the top bar. Care is taken at each step to avoid contaminating the tephra.
D. The top bar is carefully removed.
E. A specially made sheet metal plate with small sides is placed on the top bar and carefully pushed into the tephra keeping it parallel to the bedding.
F. Plate is slide into the tephra further.
G. Tephra is carefully mounded towards the middle of the plate and the plate is lifted out with the sample ready to dump into a plastic bag.
H. Process is repeated.

DR-7. XRF procedures

XRF whole rock data were obtained from three laboratories. In the Department of Mineral Sciences at the Smithsonian Institution, analyses were performed on a Philips PW 1480 spectrometer. Major elements were determined on fused glass disks prepared from 9:1 mixtures of lithium tetraborate and rock powder. Rock powders were dried for several hours at 110 °C and then weighed. Loss on ignition (LOI) determination was determined after heating at 1000 °C for one hour. Other whole rock analyses were obtained from Franklin and Marshall College. Details of instrumentation and sample preparation can be found on their website (https://www.fandm.edu/earth-environment/laboratory-facilities/xrf-and-xrd-lab). Analyses of dense juvenile material were performed at the Institute for Research on Earth Evolution (IFREE), Japan Agency for Marine Earth Science and Technology (JAMSTEC) following the procedures in Tani et al. (2005). Analyses of BHVO-1 or BHVO-2 were done in all three labs as a check of interlaboratory consistency (see DR-12).

Tani, K., Kawabata, H., Chang, Q., Sato, K., and Tatsumi, Y. (2005) Quantitative analyses of silicate major and trace elements by X-ray fluorescence spectrometer: Evaluation of analytical precision and sample preparation. Frontier Research on Earth Evolution, Vol. 2. IFREE Report for 2003-2004.

DR-8 FTIR analysis procedures

To prepare inclusions for analysis by Fourier-transform infrared spectroscopy (FTIR), crystals were initially polished on both sides to 1 μm, with at least one inclusion exposed on one side as in Nichols and Wysoczanski (2007). H_2O and CO_2 contents were measured by FTIR using a Varian FTS 7000 Spectrometer and an attached UMA600 microscope at the Institute for Research on Earth Evolution (IFREE), Japan Agency for Marine Earth Science and Technology (JAMSTEC). All analyses were collected conventionally at single spots 20 × 20 μm square, selected using the microscope, and the set up and procedures were as in Nichols et al. (2014). Where inclusions were exposed on both sides the overall measured thickness of the sample represents that of the inclusions. However, in order to ease sample preparation, in many cases inclusions were prepared so that only one surface was exposed, in which case the method described in Nichols and Wysoczanski (2007) was followed to obtain inclusion thickness. The minimum possible detectable peak on the FTIR spectra has an absorbance of 0.01 (ca. three times background), with the detection limits for the concentration of each H_2O and CO_2 species dependent on the thickness at each analyzed spot.

Following FTIR, the free-standing olivine wafers were mounted in Petropoxy 154 and analyzed by electron probe microanalysis (EPMA) on a JEOL JXA-8800 Superprobe at IFREE, JAMSTEC. This was used to measure S and Cl contents and also the major element compositions of the inclusions and their hosts, in order to allow volatile contents to be corrected for post-entrapment crystallization. Inclusions were analyzed with an accelerating voltage of 15 kV, a 10 nA beam current and defocused 3 μm beam. Counting times were 10 seconds on the peak and 5 seconds on the background for Na_2O and K_2O; 20 and 10 seconds for SiO_2, TiO_2, Al_2O_3, FeO, MgO and CaO; 30 and 10 seconds for MnO and NiO; 30 and 15 seconds for P_2O_5; 50 and 25 seconds for S; and 240 and 120 seconds for Cl. Host olivines were analyzed with an accelerating voltage of 20 kV, a 25 nA beam current and defocused 5 μm beam. Counting times were 10 seconds on the peak and 5 seconds on the background for SiO_2 and MgO; 20 and 10 seconds for TiO_2, Al_2O_3 and FeO; and 100 and 50 seconds for MnO, NiO and CaO. All analyses were performed using ZAF correction procedures. Oxides and elements were calibrated on a combination of glass and mineral standards and were checked during the measurements by interspersing measurements on secondary standards: VG-2 glass (NMNH 111240–52) (Jarosewich et al., 1980) and scapolite (NMNH R6600) (Jarosewich et al., 1980) among analyses of the inclusions; and Saint John's Island olivine (Sweatman and Long, 1969) and andradite among the olivine analyses. Major element data used here represent averages of at least 11 individual spot analyses per inclusion and at least 4 analyses of the area of the host olivine crystal surrounding the inclusion.

All inclusion compositions were corrected for post-entrapment crystallization (Roeder, 1979) by adding the host olivine back into the melt inclusion composition until the $K_D^{Fe\text{-}Mg}$ [= $(FeO/MgO)_{olivine}$ / $(FeO/MgO)_{melt\ inclusion}$)] equilibrium value of 0.3 (Roeder and Emslie, 1970) was reached. As oxygen fugacity was not directly measured in the inclusions, $Fe^{3+}/\sum Fe$ of 0.12 (Bezos and Humler, 2005) was used, with Fe^{3+} incompatible (Kelley and Cottrell, 2009). H_2O, CO_2, S and Cl were assumed to be completely incompatible in olivine during these calculations.

References

Bezos, A. and E. Humler (2005) The Fe3+/ΣFe ratios of MORB glasses and their implications for mantle melting, *Geochim. Cosmochim. Acta, 69*, 711-725 doi: 10.1016/j.gca.2004.07.026

Jarosewich, E., J. A. Nelen, and J. A. Norberg (1980) Reference Samples for Electron Microprobe Analysis, *Geostandard. Newslett.*, *4*, 43-47, doi:10.1111/j.1751-908X.1980.tb00273.x.

Kelley, K. A., and E. Cottrell (2009) Water and the oxidation state of subduction zone magmas, *Science, 325*, 605-607, doi:10.1126/science.1174156.

Nichols, A. R. L., and R. J. Wysoczanski (2007) Using micro-FTIR spectroscopy to measure volatile contents in small and unexposed inclusions hosted in olivine crystals, *Chem. Geol., 242*, 371-384, doi:10.1016/j.chemgeo.2007.04.007

Nichols, A. R. L., C. Beier, P. A. Brandl, and S. H. Krumm (2014) Geochemistry of volcanic glasses from the Louisville Seamount Trail (IODP Expedition 330): implications for eruption environments and mantle melting, *Geochem. Geophy. Geosy., 15(5)*, 1718-1738, doi:10.1002/2013GC005086

Roeder, E. (1979) Origin and significance of magmatic inclusions, *Bull. Mineral., 102*, 487-510.

Roeder, P. L., and R. F. Emslie (1970), Olivine-liquid Equilibrium, *Contrib. Mineral. Petrol., 29,* 275-289, doi:10.1007/BF00371276.

Sweatman, T. R., and J. V. P. Long (1969) Quantitative Electron-probe Microanalysis of Rock-forming Minerals, *J. Petrol.*, *10*, 332-379.

Figure DR-8-1. Image of loose K-3 olivines showing scoriaceous coatings. Most crystal have near-complete coatings. Many shown here are broken crystals oriented to show the olivine interiors.

DR-8 K-3 melt inclusion data compared to melt inclusion data from selected Kilauea eruptions.

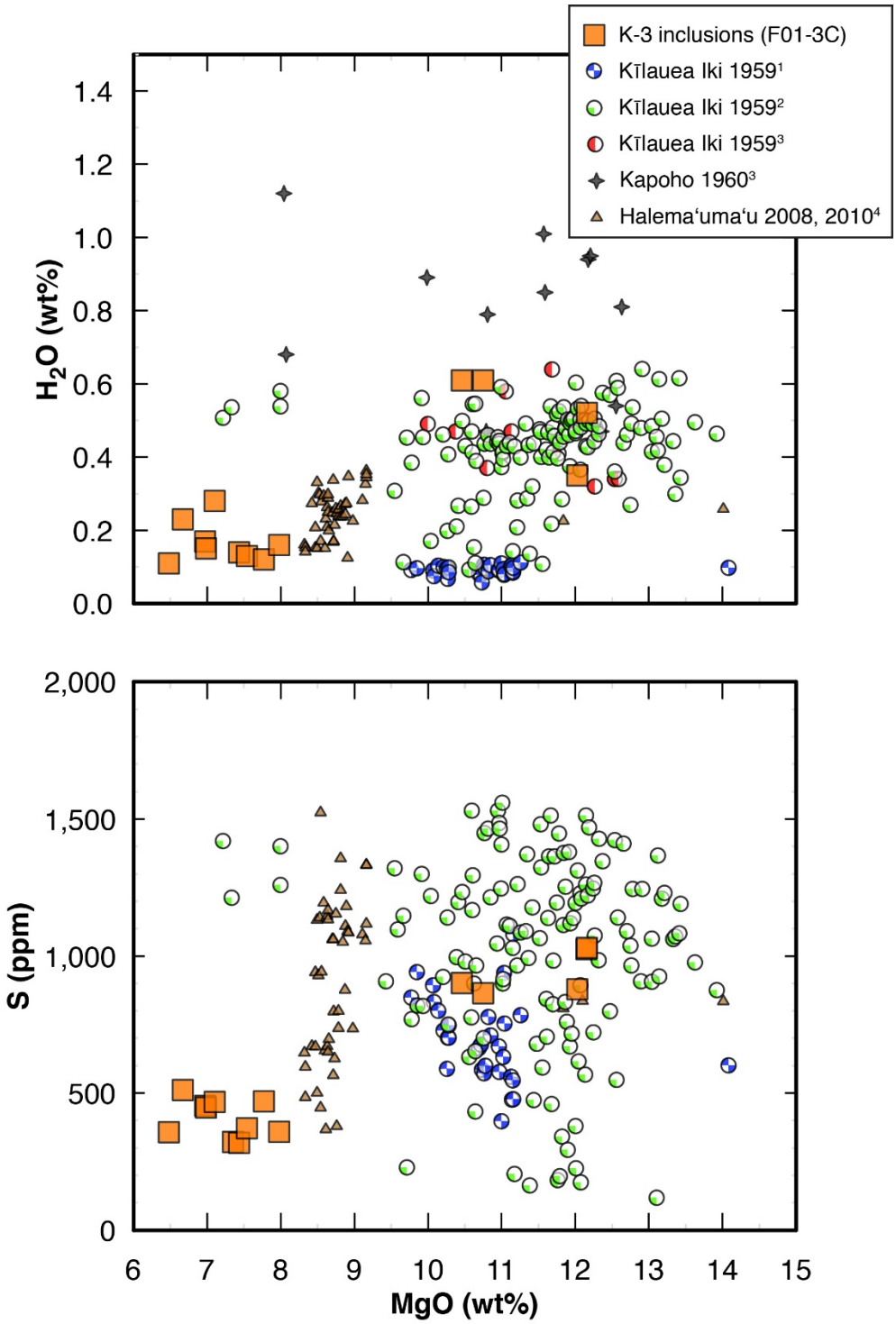

Figure DR-8-2. Post-entrapment crystallization corrected volatile contents for melt inclusions in olivines from the K-3 tephra compared to other inclusions from Kīlauea eruptions. Data sources [1]Hauri (2002), [2]Sides et al. (2014), [3]Tuohy et al. (2016), and [4]Edmonds et al. (2013).

Edmonds, M., Sides, I. R., Swanson, D. A., Werner, C., Martin, R. S., Mather, T. A., Herd, R. A., Jones, R. L., Mead, M. I., Sawyer, G., Roberts, T. J., Sutton, A. J., and Elias T., 2013, Magma storage, transport and degassing during the 2008–10 summit eruption at Kīlauea Volcano, Hawai'i. Geochimica et Cosmochimica Acta 123: 284 doi: 10.1016/j.gca.2013.05.038

Hauri, E., 2002, SIMS analysis of volatiles in silicate glasses, 2: isotopes and abundances in Hawaiian melt inclusions. Chemical Geology 183: 115 doi: 10.1016/S0009-2541(01)00374-6

Sides, I., Edmonds, M., Maclennan, J., Houghton, B. F., Swanson, D. A., and Steele-MacInnis, M. J., 2014, Magma mixing and high fountaining during the 1959 Kīlauea Iki eruption, Hawai'i. Earth and Planetary Science Letters 400: 102 doi: 10.1016/j.epsl.2014.05.024

Tuohy, R. M., Wallace P. J., Loewen, M. W., Swanson, D. A., and Kent A. J. R., 2016, Magma transport and olivine crystallization depths in Kīlauea's east rift zone inferred from experimentally rehomogenized melt inclusions. Geochimica et Cosmochimica Acta 185: 232 doi: 10.1016/j.gca.2016.04.020

DR-9. SEM and Microprobe procedures

Scanning electron micrographs were collected on a variable-pressure, field emission FEI NovaNanoSEM 600 scanning electron microscope in the Department of Mineral Sciences at the Smithsonian Institution. Operating conditions were typically 15 kV and 2-5 nA.

Electron microprobe analyses were performed on a JEOL 8900R Superprobe at 15kV and 20 nA. Primary standards for glass analyses were microcline (NMNH 143966) for potassium, manganite for manganese, apatite (NMNH 104021) for phosphorus and basalt glass A-99 (NMNH 113498) glass for all others. Basalt glass VG-2 (NMNH 111240) was analyzed throughout each run as a secondary standard. Counting times were typically 10 seconds on peak and 5 seconds on backgrounds except for P, K and Mn which were typically 20 and 10 seconds.

DR-15. Matlab model of lithic ejection via high-velocity jet

We model clast dispersal trajectories using an iterative model in Matlab. This model tracks the 2D motion of clasts of specified sizes and densities as they travel through, and are affected by, a background velocity field. The structure of the background velocity field is controlled by the diameter, orientation, and magnitude (peak velocity) of the jet, and the height and profile of the jetstream. This model tracks individual clasts of specified size and density as Lagrangian particles in a 2D velocity field. The horizontal and vertical components of velocity within the velocity field vary with horizontal and vertical position such that a high vertical velocity region (the "jet") dominates the velocity field near the vent, whereas the horizontal jetstream dominates high altitude regions, and low altitude regions far from the vent have velocities of zero; as the model is 2D and focused on interactions of particles with the jet and jet stream, the model does not consider trade winds. Particles are introduced at various radial positions at the base of the jet, with initial velocities in equilibrium with the velocity field at that position (e.g. they have the same velocity as the jet). Particle position through time is calculated as the sum of the position at the previous instant and the product of the 2D particle velocity and time step. Instantaneous 2D particle velocities are determined as the vector sum of particle momentum, gravitational, and drag forces, with the latter being determined as a function of particle size and the difference between the particle and velocity field velocities.

Background Velocity Fields

The background velocity field is determined by summing the jet and jetstream velocity fields. The height of the jetstream (or the vent) can be adjusted by shifting the jetstream velocity field up or down. The background velocity field is determined with a spatial resolution of 1 m; finer resolution is achieved through linear interpolation of the field.

Jet velocity field

The jet velocity field is described by first determining the centerline velocity of the jet, U_{jc}, as a function of distance, d, from the vent

$$U_{jc}(d) = U_{j0}\sqrt{\frac{r}{\varepsilon d}}$$

Eq. DR-15-1

where U_{j0} is the maximum initial jet velocity, ε is an entrainment coefficient (=0.16, adapted from Bernard and Wallace, 2002), and r is the vent radius. For $d \leq 8r$, this equation predicts $U_{jc}(d)$ to be greater than Uj0; we reset those values of Ujc(d) to Uj0, and consider that within that range of distance, the centerline velocity has not yet been affected (reduced) by turbulent entrainment. Variation in jet velocity at positions h away from the centerline is decays following an error function, where the outer edge of the plume, r_{out}, defines a 0-value velocity.

$$U_{jr}(d,h) = U_{jc}(d)0.5\left(1 + erf\left(\frac{r_{out} + r_{int} - 2h}{r_{out} - r_{int}}\right)\right)$$

For $d > 8r$, the interior boundary of the error function, r_{int}, equals 0 (the centerline), whereas for $d < 8r$, $r_{int}(d)$, is set by

$$r_{int}(d) = r - \frac{d}{8}$$

Eq. DR-15-3

The magnitude of the interior velocity for all conditions is set by $U_{jc}(d)$. Note that Eq. DR-15-3 defines a conical jet interior up to a distance of $8r$, that is "undisturbed," reflecting the angle at which entrainment propagates from the jet margins to the interior.

The orientation of the jet can be adjusted by a given angle away from vertical, θ, resulting in the decomposition of jet velocity U_j at position [x,y] into horizontal and vertical components of velocity U_{jx} and U_{jy} using the sine and cosine of θ.

Jetstream velocity field

The jetstream velocity is assumed to be entirely horizontal (y-component =0), and follow a parabolic profile with velocities of 0 at a specified base and top (e.g. 4000 and 11000 m, respectively), and a peak velocity of 70 m/s at, for example, 7500 m.

Particle Trajectories

Particles in the model are released at various radial positions at the base of the jet. Their horizontal and vertical positions are tracked through time as the particles are affected by drag forces and gravitational acceleration. These calculations are performed at intervals of 0.01 s, corresponding to at most 4 m of particle motion (typically <1 m of motion). We note that the only time particles are assumed to have the same 2D velocity as the local atmosphere is at their initial position.

Particles

Particles are considered to be spheres with densities of 2500 kg/m^3 and diameters ranging from 0.0125 to 0.25 m. Particle momentum is determined as the product of mass and velocity.

Drag force

Drag is calculated as a function of the relative velocity, U_{rel}, between a given particle and the velocity field at that position, with a particle Reynolds number dependent drag coefficient C_d (ranging from 0.4 for Re<4×10^5 to 0.1 for Re>6×10^5). The drag force, F_{drag}, is given by

$$F_{drag} = 0.5 C_d \rho_{air} A (U_{rel})^2$$

Eq. DR-15-4

Where ρ_{air} is the density of air and A is the particle cross sectional area. The drag force has horizontal and vertical components determined by the orientation of U_{rel}. Acceleration of a particle in response to drag is proportional to F_{drag} and inversely proportional to particle mass.

Initial conditions

Particles are initially "released" in the model at the vent, e.g. the base of the jet, at radial positions varying from the center to 0.8r; note that positions on the "left" and "right" sides of the center are considered, as inclined jets will not have symmetrical horizontal and vertical components of velocity. Particles have velocities with initial magnitude equal to that of the jet, but the orientation is allowed to vary over a range of ±7.5° from that of the jet to account for dispersion of the particles.

References

Bernard, P.S. and Wallace, J.M., 2002. Turbulent Flow. John Wiley and Sons, Hoboken. 497 pages.